Taylor & Francis
Taylor & Francis Group

∂ OPEN ACCESS | Check for updates

Experimental and numerical modelling of shear bonding between asphalt layers

Denis Jelagin [a], Erik Olsson [b], Christiane Raab[c] and Manfred N. Partl [d]

[a]Department of Civil and Architectural Engineering, KTH – Royal Institute of Technology, Stockholm, Sweden; [b]Department Engineering Sciences and Mathematics, Luleå University of Technology, Luleå, Sweden; [c]Concrete and Asphalt, Empa, Swiss Federal Laboratories for Material Science and Technology, Duebendorf, Switzerland; [d]PaRRC Partl Road Research Consulting, Oeschgen, Switzerland

ABSTRACT

Interlayers in asphalt pavements are potential structural damage initiators. In order to better understand the quantitative role of interlayer parameters, such as surface roughness, binder type, binder content and loading type on interlayer shear strength, this paper focuses on the effects of particle interlock and contact conditions on interlayer strength through experimental and numerical modelling. Experimentally, interlayer shear box strength tests on a model material consisting of stiff binder blended with steel balls are performed with and without normal force confinement. A Discrete Element method model of the test is developed using measurements of the model material for calibrating the contact law and for validating the model. It is shown that this model captures adequately the measured force-displacement response of the specimens. It is thus a feasible starting point for numerically and experimentally studying the role of binder and tack coat regarding interlayer shear strength of real asphalt layers.

1. Introduction

Asphalt pavements are orthotropic multilayered structures that are expected to carry repeated static or dynamic vertical traffic loads under complex climatic and environmental conditions. Hence, roads are subject to different kinds of horizontal shear stresses which may affect the interlayer bonding and therefore the bearing capacity and durability of the whole pavement structure. Interlayer shear stresses may be induced by bending in case of weak flexible subgrades due to design and construction deficiencies. Particularly under heavy traffic, they may also result from horizontal tire-pavement interaction during breaking and acceleration or by centrifugal forces in curves and roundabouts. Horizontal interlayer stresses are not necessarily traffic-induced and may occur in case of steep slopes and ramps or settlements from later trenching or pavement patching. From a purely climatic and environmental point of view, different relative thermal contraction and expansion behaviour of the pavement layers may also lead to horizontal interlayer shear stresses.

Due to the fact that interlayer bond plays such an important role, considerable research on this topic has been performed for many years worldwide. In fact, different test methods for characterising the interlayer shear behaviour have been developed and standardised. Direct shear, indirect shear, torsion, bending, double shear test and numerous other tests with and without normal force dilatation confinement have been proposed as listed in the papers by Raab et al. (2009) and Canestrari et al. (2013).

CONTACT Denis Jelagin ✉ jelagin@kth.se

Extensive work has been done internationally by the International Union of Laboratories and Experts in Construction Materials, Systems and Structures RILEM (Canestrari et al., 2021) as well as nationally e.g. (Ascher & Wellner, 2007; Diakhaté et al., 2006; Salinas et al., 2013; Zofka et al., 2015).

Most common is the interlayer quasistatic indirect shear test according to Leutner (1979) where a horizontally laid core is vertically sheared with a semicircular yoke until failure at the interlayer occurs. No normal force is applied, but a reasonable ranking between different pavements can be achieved as already shown sometimes ago by Raab and Partl (1998). For practical reasons, ranking data can be analysed on a larger scale by appropriate statistically based modelling as demonstrated by Raab et al. (2013).

Since the Leutner type of test is a quasistatic shear strength test, it is only able to characterise interlayer shear with respect to failure simulating an unrealistic situation with large shear deformation without normal forces that is not expected to occur during service in a pavement. Hence, attempts have been made during the last decade to create tests that allow characterising and quantifying interlayer shear properties under repeated traffic-like loading (Ascher & Wellner, 2007; Diakhaté et al., 2006; Wellner & Wistuba, 2016; Zofka et al., 2015). However, due to the complexity and engineering problems, no internationally accepted test protocol is available so far.

One key issue regarding interlayer shear properties is the effect and influence of the interface roughness which is partly governed by the maximum aggregate sizes of the top and lower layer, or by the texture from milling the old pavement surface for a new overlay. Due to practical problems in measuring this roughness, only little focus has been devoted up to now for determining and studying this interlayer characteristic which is very relevant for both, design and construction. An attempt has been made in a PhD thesis by Ferrotti (2007) applying computer tomography and fractal analysis. Main results have been published by Santagata et al. (2008). The lack of computational and experimental tools capable of capturing the effect of those geometrical parameters on the interlayer shear behaviour is particularly disappointing since it precludes the optimisation of interlayers from fundamental mechanical considerations.

In fact, the mechanism of interlayer shear in presence of bituminous binder is quite complex as shown schematically in Figure 1. It is not only characterised by horizontal displacement but also by vertical dilatation effects that are hindered by the tension adhesive and cohesive properties of the bitumen. In a first stage one would expect mainly short sliding in a horizontal plane (A) until the majority of aggregates on the top and bottom interlayer surface interlock by squeezing the bitumen film between the interlocking particles on top and bottom (B). Thereafter particles in the upper layer slide upwards along the bottom particles while being hold back by the bitumen film on the initial sliding plane (C). This results in an increase of measured shear force and in reduced horizontal displacement up to the point where the bitumen film on the initial sliding plane is no longer able to hold back the upwards movement of the top particles (D). The consequence is that the upward particles gradually reach the top of the bottom particles with reduced effort, in this way producing maximum dilatancy and now sliding with minimal force (E) until falling into the next valley of the roughness texture (F) before the next dilatancy cycle starts.

It is clear that the schematic example in Figure 1 is a strong oversimplification of the interlayer shear bond mechanism, since it ignores normal force and real surface texture of both the top and bottom layer. However, it may start as a starting point for refining the understanding and modelling of the micromechanical shear bonding effects between asphalt layers.

In order to study the effect of interface roughness under horizontal shear, an experimental modelling effort with a shear box has been undertaken by Raab et al. (2012) with unbound and bound model layers, each made of single-sized steel balls as aggregate surrogate but different steel ball size. It clearly showed the influence of different ratios between the maximum aggregate sizes on the top and bottom layer. Another attempt for improving the understanding the effect of interface roughness was performed with discrete element modelling DEM by Ghafoori Roozbahany and Partl (2019), showing that compacting a coarse grade asphalt mixture on a rough bottom surface may have a positive
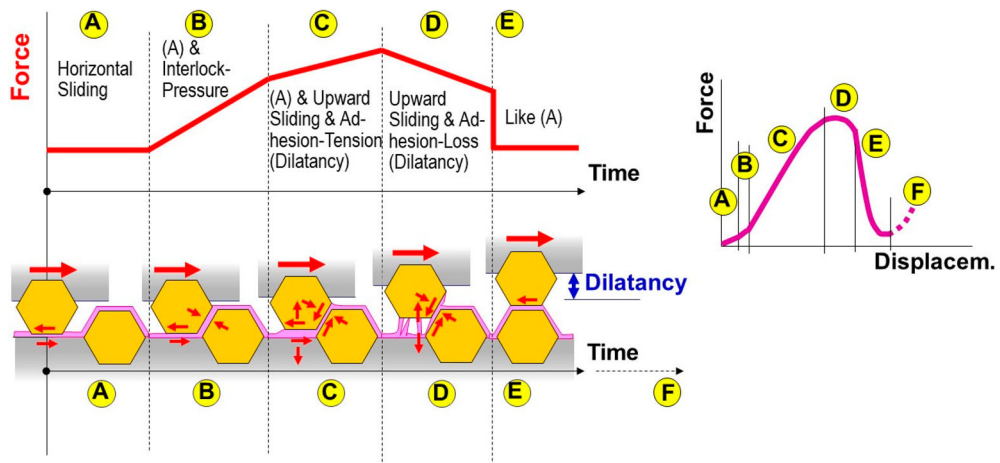
Figure 1. Schematic evolution of quasi-static shear force-displacement characteristic of an interlayer with equal top and bottom layer roughness showing the bonding and sliding effect in case of a thin bitumen film on top of the bottom layer and no action of normal force.

effect in blocking horizontal displacements and in this way improve functionality of joints in asphalt pavements.

Both papers were the motivation for this paper which intends to link the experimental modelling approach with refined DEM-driven numerical modelling. Hence, taking into account the results on the model layers by Raab et al. (2012), the aim of this work is to propose a computational tool based on DEM for evaluating the effect of interlock and contact conditions on the interlayer strength and for investigating the influence of interlayer surface geometries, binder and normal forces on the interface characteristics. This is considered particularly relevant for designing noise-reducing surface layers, which tend to be more and more composed of gradations with small nominal maximum aggregate sizes. It is also important with respect to surface milling for rehabilitation and the question of required tack coat film thickness.

2. Methodology

Experimental modelling results from shear box tests, as described by Raab et al. (2012) were compared with numerical modelling for validating the refined DEM computational approach by Olsson et al. (2019) in case of interlayer shear to improve the understanding of the mechanical processes during testing by studying a selected set of influence parameters. This was triggered by the fact that computational modelling is more versatile and less laborious than experiments, thus allowing the study of more specific cases, especially in respect to interlayer surface geometries, normal forces, size effects and influence of binder properties. Table 1 provides an overview on the experimental modelling parameters for which shear box test results were available. In what follows different ball size combinations tested and simulated are denoted by the ratios with the top layer ball sizes in mm divided by the bottom layer ball sizes, i.e. (5.5/9.5) denotes the material having 5.5 mm balls on top of 9.5 mm.

The measurements from the tests summarised in Table 1 were used to calibrate the material parameters in the DEM model as well as to validate the developed model. Namely, the measurements obtained for (9.5/9.5) material with and without binder were used for material parameter calibration. The calibrated model has been used then to simulate the shear box tests on (5.5/5.5) and (5.5/9.5) materials for both bound and unbound cases, and the model's capability to capture the experimental observations has been examined.

Table 1. Material and loading parameters for experimental modelling with shear box testing and DEM calibration and validation.

Type of test	Steel ball sizes top/bottom layer [mm]	Normal confining stress [kPa]	No. of tests bound materials	No. of tests unbound materials
	(5.5/5.5)	100	6	2
		400	6	3
Shear box	(9.5/9.5)	100	6	3
		400	6	3
	(5.5/9.5)	100	6	2
		400	6	2

Table 2. Modelling parameters for the DEM parametric study on the effect of particle size ratios on shear strength of bound materials. For each configuration, three individual simulations were performed.

Ball sizes top layer, [mm]	2.5	3.75	5	5.5	7.5	5.5	9.5	10	13
Ball sizes bottom layer, [mm]	10	10	10	9.5	10	5.5	9.5	10	10
Top/bottom size ratio	0.25	0.375	0.5	0.58	0.75	1	1	1	1.3
Normal stress, σ_n, [kPa]					100, 400				

Table 3. Modelling parameters for the DEM parametric study on the effect of normal stress on the shear strength of bound materials. For each configuration, three individual simulations were made.

Normal stress, σ_n [kPa]	0	100	400	800
Ball sizes top/bottom layer [mm]		(5.5/5.5), (5.5/9.5), (9.5/9.5)		

The developed DEM model has furthermore been used to perform a brief parametric study in order to examine the effect of top to bottom size ratios and of normal pressure magnitude on interlayer shear strength for the specimens with bound materials. The ball size combinations and normal pressure levels examined in this study are summarised in Tables 2 and 3. As visible in Table 1 and discussed in some detail in section 2.1 below, several test repetitions were performed for each material and loading case. The experimental results were then averaged with the procedure detailed in section 2.1. Numerically, for each of the materials/load cases evaluated, three DEM runs were performed with new randomly generated particle arrangements; the results were averaged following the procedure identical to the one used in the experiments.

2.1. Experimental modelling

The model material used consisted of bituminous layers made of single-sized steel balls and a hard 10/20 penetration graded bitumen in order to ensure sufficient stability for testing at 20°C. Two different sizes of steel balls with diameters of Ø 5.5 and Ø 9.5 mm were chosen and considered as representative of the mineral aggregates in a pavement. In fact, the steel ball diameters with a ratio of 1:2 were selected since, in practice, this combination proofed to be the most relevant nominal maximal aggregate size ratio between surface and binder courses. In this way, double-layered cylindrical specimens with a diameter Ø of 100 mm, a height of 35 mm, a bitumen content of approx. 37.5 vol-% and an air void content of 0% were produced by filling steel balls and 160°C hot bitumen into preheated moulds. After finishing the first layer and cooling down to ambient temperature, the mould was flipped over and placed on a wet sand bed with the original upper side facing down as to obtain a clear flat interface, before applying the second layer onto the first one.

The double-layered specimens were fabricated with different combinations of steel ball layers such as 5.5/5.5, 5.5/9.5 and 9.5/9.5 as shown in Table 2. In addition, double-layered unbound specimen without binder was also tested. Figure 2 depicts a specimen with the ratio of 5.5 mm for the top and 9.5 mm for the bottom after separation.

Testing was performed with the shear box test device from the Swiss Federal Institute of Technology ETH in Zurich which comprises two half boxes with cylindrical metal rings of Ø 100 mm for

Figure 2. Bound specimen with the ratio of 5.5 mm for the top and 9.5 mm for the bottom after testing and separation.

holding the specimen as shown in Figure 3. The lower half box is held tight while the upper one is fixed on a sliding table, which is moved horizontally at constant rate of 2.5 mm/min. The vertical load normal to the shear plane is applied hydraulically as shown in Figure 3. Horizontal and vertical displacements are measured using displacement sensors. Testing was done at 20°C and all specimens had been conditioned for 8 h prior to testing.

The maximum shear forces were derived from the shear force-deformation curves. For obtaining mean curves, the single curves were normalised relative to maximum shear force and corresponding shear deformation and averaged before being back calculated to real units.

2.2. Numerical modelling

In asphalt pavement structures, the shear and compressive loads at the interlayer are transferred mainly by contact forces between the aggregates while tensile loads are transferred through the binder film between the aggregates as schematically shown in Figure 1. These local interaction forces between the aggregates are dependent on the aggregate size distribution, the aggregate contact stiffnesses and the mechanical properties of the binder. The modelling framework should explicitly account for these effects to obtain the best computational insights and to be able to reliably investigate the effect of the parameters. The Discrete Element Method (DEM), originally developed by Cundall and Strack (1979) is the natural choice for such a framework as each single aggregate, denoted as a particle, is modelled as a separate object and their motion is governed by the local contact forces.

The DEM software used presently is an in-house code named DEMsim developed for studying a variety of applications, including road materials. The framework has been presented in Olsson et al. (2019, 2020), is implemented in C++ and is publicly available at github (www.github.com/erolsson/DEMsim). The framework uses the standard formulation in DEM for integrating the translational and rotational equations of motion.

One of the most important concepts in DEM is the calculation of contact forces between two particles as this is one of the key issues that governs the physics of the problem. In the present case, the contact forces are divided into two contributions, one from contact between the aggregates and one additional contribution from the binder. A sketch of the contact interaction is shown in Figure 4 where quantities for calculating the contact forces are defined.
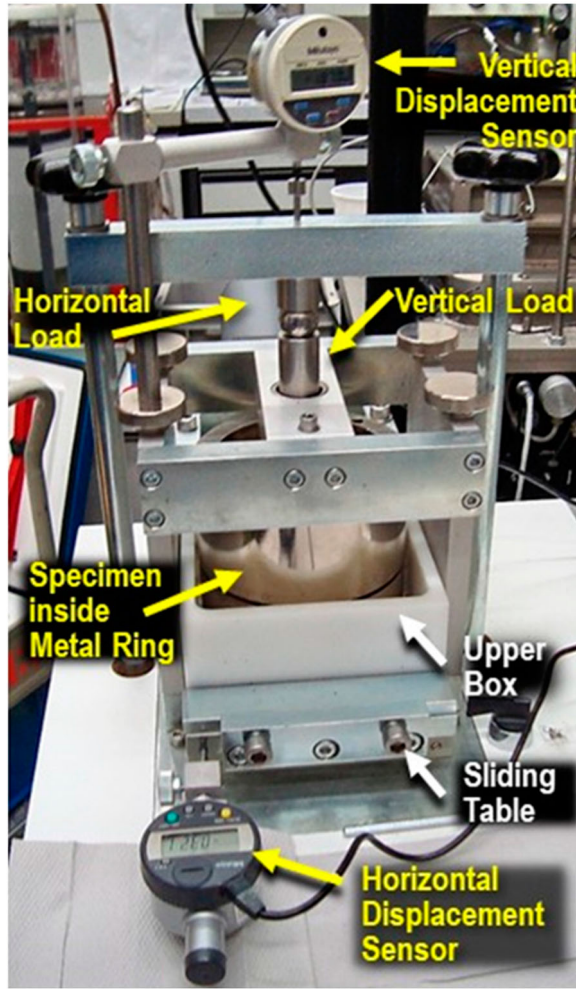
Figure 3. Shear box device.

It is convenient to calculate the increment in the forces in terms of the increment in overlap Δh as well as the increment in the tangential displacement vector $\Delta \delta_T \hat{t}$ that is directly perpendicular to the contact normal $\hat{n}$. For the normal contact force F_N, the contribution from direct contact between the aggregates, F_{Na}, can straightforwardly be modelled using contact mechanics since spherical steel balls are used as a model material. Before any notable plastic contact deformations occur, the contact behaviour is assumed to be fully elastic, and the increment in force is given by Hertz contact theory (Hertz, 1881) by

$$\Delta F_{Na} = 2E_0 \sqrt{R_0 h} \Delta h \tag{1}$$

where E_0 and R_0 are the effective Young's modulus and effective particle radius for the contact. They are defined as

$$\frac{1}{E_0} = \frac{(1 - v_1^2)}{E_1} + \frac{(1 - v_2^2)}{E_2} \tag{2}$$

and

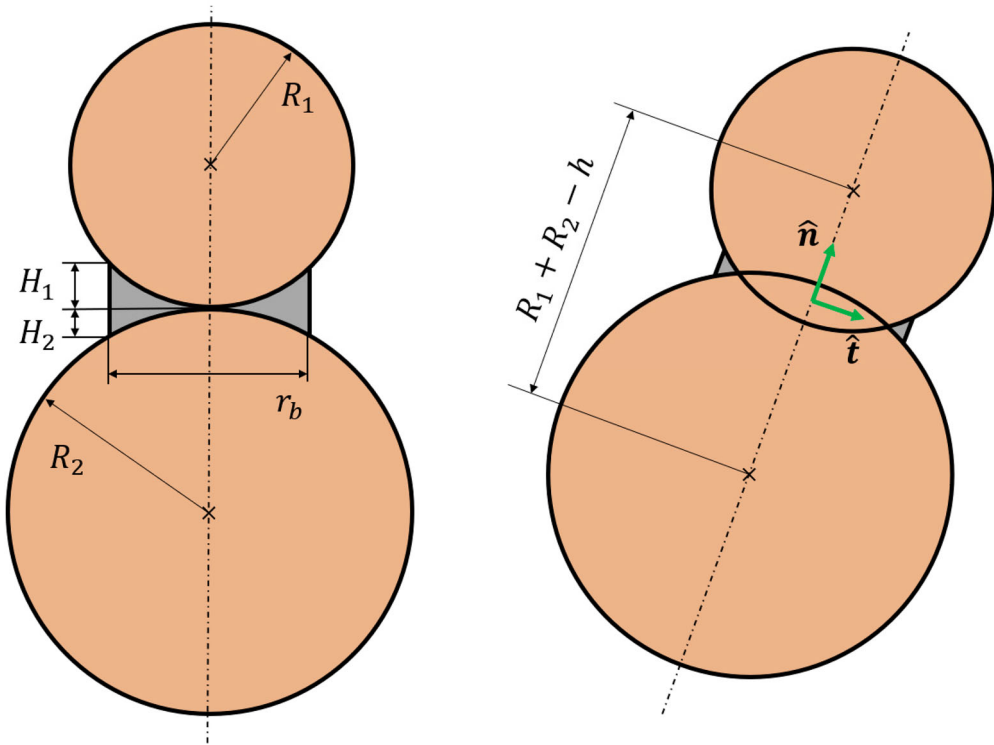$$\frac{1}{R_0} = \frac{1}{R_1} + \frac{1}{R_2} \tag{3}$$

Figure 4. Sketch of the two particles contact interaction in presence of the binder; the binder is coloured in grey. To the left is when the particles just touch each other when geometrical parameters of the binder can be defined. To the right is a deformed configuration with the normal $\hat{n}$ and tangential $\hat{t}$ directions defined as well as the overlap h.

with E_i and ν_i being Young's modulus and Poisson's ratio of the spherical particle i and R_i is its radius. Equations (1)–(3) are also valid in the case of contact between one particle and a rigid wall by setting E_i and R_i to infinity for the rigid and flat object.

At larger contact deformations, the effect of plasticity on the contact behaviour becomes significant and in this regime the increment in contact force is linear according to the analysis by Storåkers et al. (1997) if ideal plasticity is assumed

$$\Delta F_{Na} = 6\pi c^2 R_0 \sigma_Y \Delta h \tag{4}$$

where the parameter c^2 takes on the value $c^2 = 1.43$ and σ_Y is the yield stress of the material, presently assumed to be 500 MPa. The indentation depth h_Y where the behaviour is changed from elastic (Equation [1]) to plastic (Equation [4]), is determined so that a continuous derivative in the force-overlap relationship is obtained as shown schematically in Figure 4. Using $E = 200$GPa, $\nu = 0.3$ and $\sigma_Y = 500$ MPa, this value becomes $0.0037R_0$ for particle–particle contacts and $0.00094R_0$ for particle-surface contacts.

The main reason for introducing plasticity in the present case is to limit the contact stiffness, and not model elastic-plastic effects in detail as they are expected to be small. The contact stiffness has to be limited as the time step to have a stable solution in DEM is proportional to $\sqrt{m/k}$ where m is the mass of the particle and k the contact stiffness. At unloading-reloading after the contact has deformed plastically, the behaviour is elastic, and Equation (1) is applicable. A sketch of the normal force behaviour for aggregate-aggregate contact is sketched in Figure 5.

Tangential forces are as important as the normal forces for capturing the mechanical behaviour and especially for this problem, where shearing is the main deformation mode. In order to account for this fact, a standard stick-slip model is used as outlined below. At the beginning of the time increment,
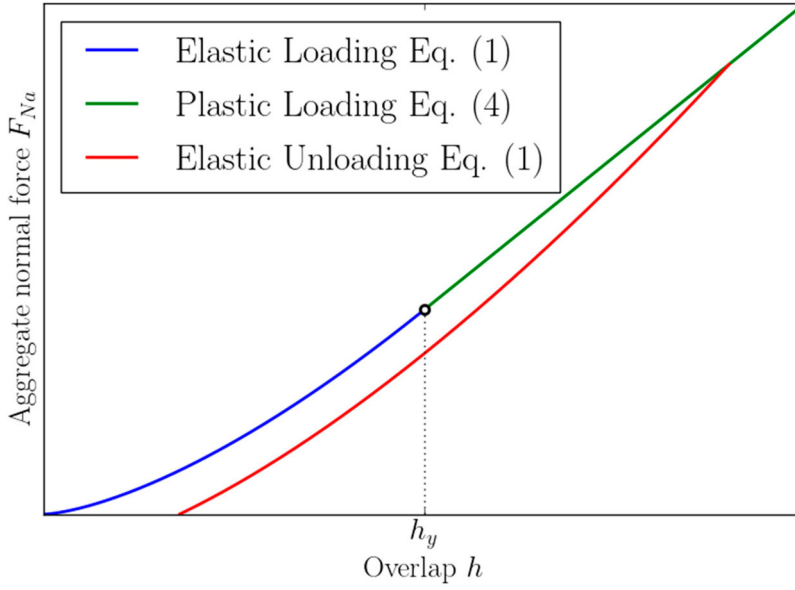
Figure 5. Sketch of the force-overlap relation with elastic loading, followed by plastic loading and elastic unloading when the contact has been plastically deformed.

the tangential displacement vector from the previous time increment is projected on the tangential direction ensuring that the tangential force always is perpendicular to the normal direction followed by adding the current increment in tangential displacement $\Delta \delta_T \hat{t}$. A trial tangential force is calculated

$$\boldsymbol{F_{Ta}} = k_{Ta} \delta_T \hat{t} \tag{5}$$

where k_{Ta} is the tangential contact stiffness. This stiffness is in theory dependent on the normal force, (Mindlin, 1949; Olsson & Larsson, 2014), but as such a model is cumbersome in DEM simulations, (Thornton et al., 2011; Zhang & Vu-Quoc, 2007), a constant stiffness is used where it is assumed that the radius of the contact area, a is 1/1000 of the effective particle radius R_0. This approximative model is justified in this application by the fact that large shear deformation occurs and then the sliding behaviour is of most importance. The contact stiffness is then given by Equation (6) which is approximately valid for both elastic contacts (Mindlin, 1949) and for plastic contacts (Olsson & Larsson, 2014).

$$k_{Ta} = \frac{E}{2(1+\nu)} \frac{8a}{2-\nu} \tag{6}$$

where a denotes the contact radius; as discussed above $a = 0.001 R_0$. If the norm of this force exceeds the Coulomb limit μF_{Na} with μ being the friction coefficient, the contact is assumed to be in a slipping state and the tangential displacement δ_T is set according to

$$\delta_T = \frac{\mu F_{Na}}{k_{Ta}} \tag{7}$$

before using Equation (5) a second time to calculate the final tangential force. The coefficient of friction, μ, is viewed as a constant fitting parameter and will be calibrated using the experiments on unbound materials.

The bituminous binder will add extra stiffness to the contact and additional normal F_{Nb} and tangential $\boldsymbol{F_{Tb}}$ binder forces are added to the contact force. A problem with similar geometry but for a completely different application, lithium-ion batteries, were analysed by Gudmundson and Larsson

Table 4. Summary of parameters defining the contact behaviour.

Material	Parameter	Value	Comment
Steel	Youngs modulus E	200 GPa	Assumed, based on standard values for steel
	Poisson's ratio ν	0.3	Assumed, based on standard values for steel
	Yield stress σ_Y	500 MPa	Assumed, based on standard values for steel
	Friction coefficient μ	0.8	Calibrated using unbound data for (9.5/9.5) balls
Binder	Stiffness K	5 MPa	Calibrated using bound data for (9.5/9.5) balls
	Failure stress σ_F	15 MPa	Calibrated using bound data for (9.5/9.5) balls

(2021). Based on their work, the normal k_{Nb} and tangential k_{Tb} binder stiffness can be calculated using the geometrical quantities in Figure 4.

$$k_{Nb} = K \frac{(1 - \nu_b)}{(1 + \nu_b)(1 - 2\nu_b)} \frac{\pi r_b^2}{(H_1 + H_2)} \tag{8}$$

$$k_{Tb} = K \frac{1}{(1 + \nu_b)} \frac{\pi r_b^2}{(H_1 + H_2)} \tag{9}$$

where ν_b is the Poisson's ratio of the binder which is assumed to be 0.3 and K is a stiffness calibration parameter with the dimension of stress. The binder radius r_b is assumed to be 20% of the effective radius R_0. The analysis is not dependent on this value as the stiffness K will then change accordingly to obtain the same stiffnesses.

When the maximum principal stress, σ_1, in the binder, has reached the tensile fracture stress of the binder, σ_F, the binder has fractured and all forces in the binder are set to zero. The maximum principal stress is calculated using Mohr's circle by

$$\sigma_1 = \frac{1}{\pi r_b^2} \left[-\frac{F_{Nb}}{2} + \sqrt{\left(\frac{F_{Nb}}{2}\right)^2 + \boldsymbol{F_{Tb}}^2} \right] \tag{10}$$

where it is assumed that a positive binder normal force F_{Nb} is compressive and $\boldsymbol{F_{Tb}}$ denotes the magnitude of the tangential binder force.

At first glance, the contact model presented in Equations (1)–(10) might seem complex, but it contains only three calibration parameters, the friction coefficient μ, the binder stiffness K and the binder fracture stress σ_F. These three parameters will be calibrated in the next section using the experiments with steel balls of 9.5 mm size in both layers. A summary of all model parameters, their values and how they are determined is given in Table 4.

The DEM simulations follow the experimental procedure as closely as possible. The bottom layer is filled with steel balls to half of the height of the cylinder, and the first layer is bonded together using the binder model described above. In a second step, the cylinder is flipped upside-down, and a second layer of steel balls is filled above the flat interface. Finally, binder is applied to this layer and the virtual shear testing starts where a confining stress σ_n is applied to the top and bottom of the specimen simultaneously as the cylinders are moved perpendicular to each other while the reaction shear force is registered. A visualisation of this procedure is shown in Figure 6. For each simulated case, three individual simulations are performed, and the mean of those simulations is reported as the results.

3. Results and discussion

In this section, results concerning the stress-displacement responses of specimens in shear box tests are examined first as observed experimentally and numerically. The (nominal) shear stress is defined as $4Q/\pi d^2$ where Q is the shear force and d is the diameter of the specimen. The experimental and modelling results presented in Figures 7 and 8 are average values of 2–3 measurements and 3 simulations
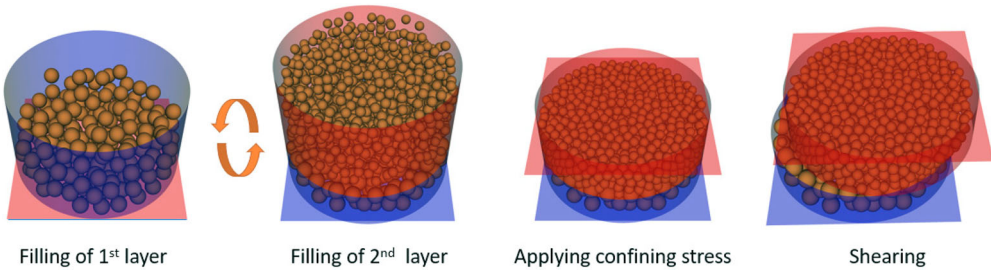
Filling of 1st layer   Filling of 2nd layer   Applying confining stress   Shearing
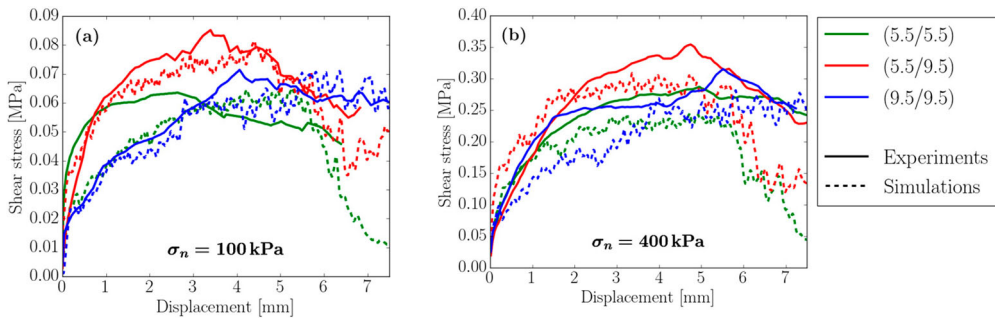
Figure 6. Main steps of the simulation procedure.

Figure 7. Measured and simulated stress-displacement response in shear box tests on unbound materials: (a) $\sigma_n = 100$kPa; (b) $\sigma_n = 400$kPa.

respectively. In Figure 7(a) and (b) the shear stress-displacement responses of unbound specimens at confining stresses of $\sigma_n = 100$ and 400 kPa are presented. A small parametric study with different friction coefficient showed that could accurately fit the data where both layers consist of large (9.5/9.5) steel balls. It may be seen that the proposed modelling approach is in good qualitative and quantitative agreement with the measurements, at least until the peak load levels. In particular, calculated maximum force values are within 20% of the measured ones for all cases examined. The effect of increasing confining stress on the specimens' shear strength is also captured well with both experimental and modelling results, indicating that the strength of unbound specimens increases approximately linear with vertical confining stress. With respect to the effect of particle sizes, the calculated maximum load for (5.5/9.5) material is approximately 15–25% higher as compared to the ones calculated for (5.5/5.5) and (9.5/.9.5) materials. This may be compared with 15–30% increase observed for (5.5/9.5) material experimentally. At the same time, DEM model overestimates the decrease of force in the post peak region at shear displacement above 5 mm which may be explained by the fact that small particles escape the confining cylinders at higher rate in the model compared to experiments. As it is also seen, the calculated force-displacement curves fluctuate somewhat more as compared to the experimental ones, which may be explained by the lack of local dampening mechanisms in the model. In spite of those shortcomings, the model captures the experiments well (until peak loads) which indicates that the contact law parameters for ball-to-ball interactions are chosen adequately.

In Figure 8(a) and (b) stress-displacement responses of the specimens with bound material are presented in the same manner as in Figure 7. Also, in this case a small parametric study was conducted using two layers of larger balls to determine the calibration parameters K and σ_F. A binder stiffness $K = 5$MPa and a binder fracture stress $\sigma_F = 15$MPa was found to capture the behaviour of the (9.5/9.5) experiments nicely. It must be noted that those values are directly dependent on the assumed geometry of the binder bond and should therefore not be regarded in any way as material properties of the binder.
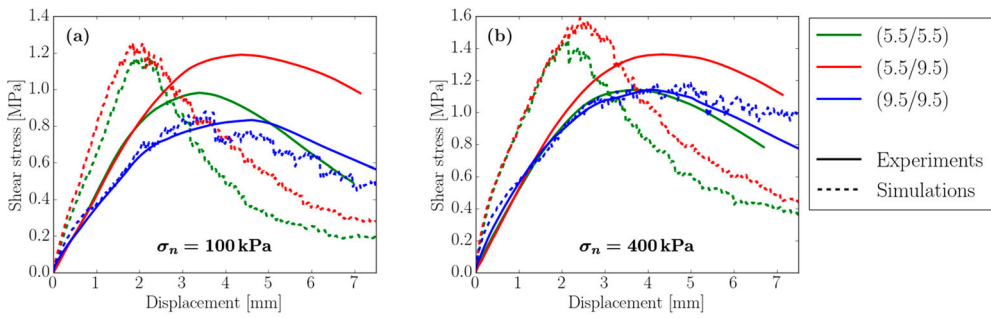
Figure 8. Measured and simulated stress-displacement response in shear box tests on bound materials: (a) $\sigma_n = 100$kPa; (b) $\sigma_n = 400$kPa.
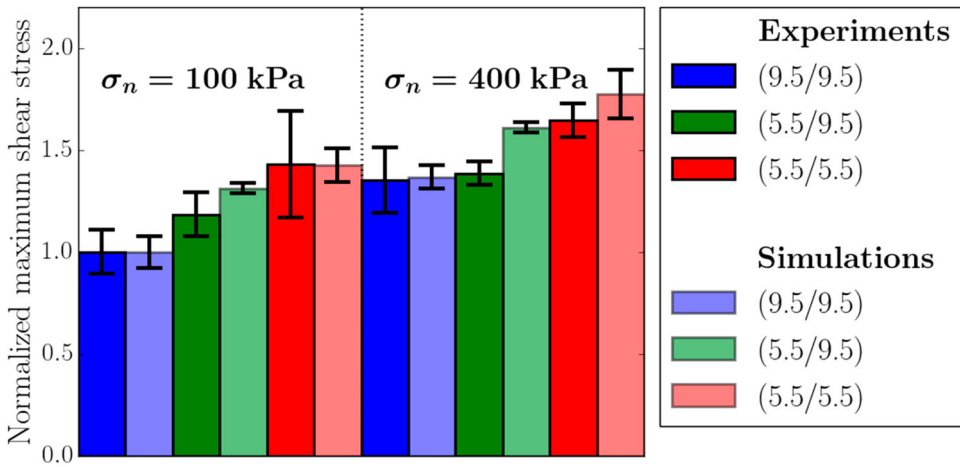

Figure 9. Measured and simulated maximum force levels attained in shear box tests on bound materials. The results are presented normalised with the maximum shear stress obtained at (9.5/9.5) combination and $\sigma_n = 100$ kPa.

Similar to the results in Figure 7, it was observed that while maximum load levels are captured reasonably well by the model, the post-peak curves are significantly underestimated except for the (9.5/9.5) material. Furthermore, the initial stiffness of the (5.5/5.5) and (5.5/9.5) materials is somewhat overestimated by the model. These discrepancies are attributed to the postulated binder stiffness model in Equations (8)–(10). This part of contact laws need to be developed further in future studies incorporating viscoelastic effects and improving the description of the binder bond geometry. At the same time, the model captures well the influence of vertical pressure and ball sizes on the specimen's strength, i.e. maximum shear force measured in the test. This is illustrated further in Figure 9 where the calculated and measured specimens' strength is presented, normalised with the strength measured for (9.5/9.5) material at 100 kPa confining stress. Note, that the maximum shear forces are significantly higher in the bound than in the unbound case and less depending on the confining stress, thus, clearly demonstrating the positive role of binder. The experimental and simulation bars in Figure 9 represent the average value of 3 tests and 3 simulations respectively. Also in Figure 9, standard deviation in maximum shear stress for each material and stress level are indicated. As seen in Figure 9, for all cases except (5.5/5.5) material at 400 kPa confining pressure, the DEM and experimental results are in good agreement, i.e. within experimental scatter. The maximum deviation between the modelling and experimental results is observed to be approximately 20% for the case of (5.5/5.5) material at 400 kPa confining pressure, which is remarkable given that the same set of material parameters is used in all simulations.
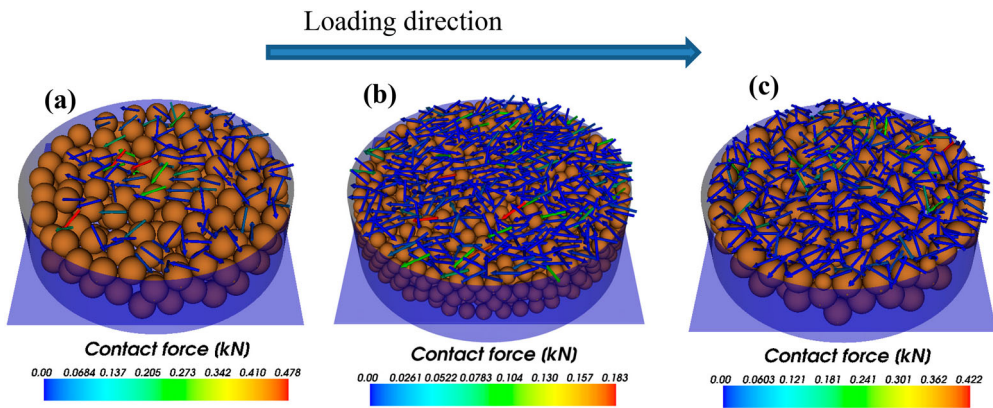
Figure 10. Distribution of contact shear forces at the shear plane of bound materials observed at peak load and at $\sigma_n = 400$kPa; (a) (9.5/9.5) combination (b) (5.5/5.5) combination (c) (5.5/9.5) combination.

In order to gain some micromechanical insight into interlayer shear phenomena, the distributions of shear contact forces at the shear plane are presented in Figure 10(a–c) for the (9.5/9.5), (5.5/5.5) and (5.5/9.5) materials at 400 kPa confining stress. The distributions in Figure 10 are shown at peak load values, with arrows indicating the orientation of the shear contact force for each aggregate and arrow colour indicating the force magnitude. The balls without arrows indicate broken bonds. As may be seen the (5.5/5.5) material results in smaller contact forces as compared to both (5.5/9.5) and (9.5/9.5) materials. Furthermore, in the (9.5/9.5) material several large pockets of debonded material exist in contrast to the other two cases, where the damage is more uniformly distributed. Accordingly, the high shear strength of the (5.5/9.5) material may be explained by its ability to distribute macro-scale loads in a more uniform manner. Whereas the comparatively low strength of the (9.5/9.5) material as compared to the (5.5/5.5) case may be due to the broken bonds that are concentrated on the left border of the specimen, thus suggesting that a now reduced area of the specimen is carrying the maximum shear load. Hence, the cases with the same top/bottom ratio but different ball sizes resulted in different maximum shear forces.

The results presented above indicate that the developed computational procedure captures well the effect of particle sizes and confining stress on the shear strength of the specimens. Furthermore, the results presented in Figure 10 illustrate the advantage of analysing experimental results with DEM models as they allow quantifying the effect of meso-scale parameters of the interlayer, such as surface roughness, binder stiffness and strength on materials shear strength.

For the accurate prediction of interlayer properties precise contact law parameters, in terms of aggregate stiffness, binder properties and friction coefficient are essential. In this context, the experimental modelling is also particularly instrumental as it allows to remove some experimental uncertainties associated with the testing of real asphalt mixtures, such as aggregate shape, local distributions of binder, type of binder and air voids. Accordingly, those measurements provide a crucial input for the identification of contact law parameters. In this study, the test results for the (9.5/9.5) material were used to determine the three calibration parameters: the friction coefficient μ, the binder stiffness K and the binder fracture stress σ_F. This approach may be refined further to better account for the influence of aggregate sizes on the bituminous bond strength and stiffness, by incorporating an additional calibration based on the tests with (5.5/5.5) material. This refinement will be performed as a part of future studies.

When representative contact law parameters are identified, the DEM modelling may be used to extrapolate the experimental findings over a wider range of conditions (e.g. in terms of pressure levels and particle size combinations). In order to examine the feasibility of using the DEM to evaluate the effect of geometrical interlayer parameters and of vertical confining loads on the interlayer
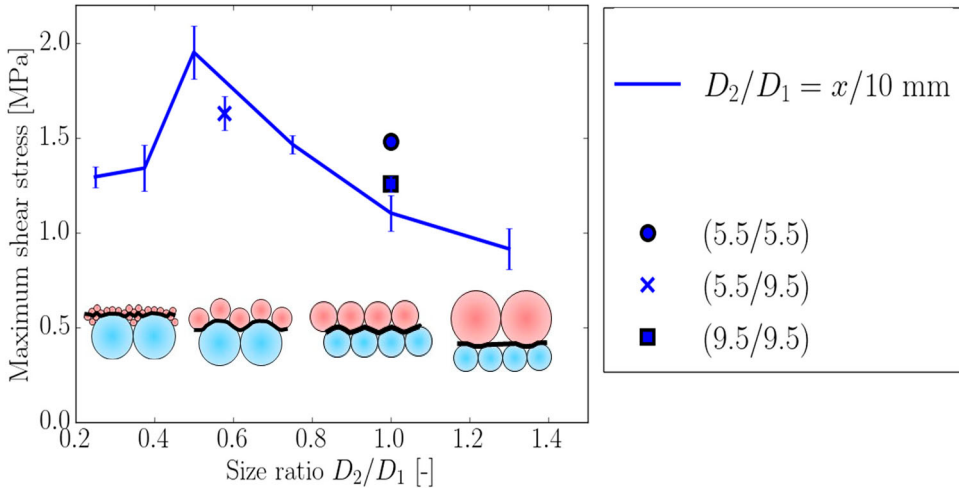
Figure 11. Maximum shear stress in simulated shear box tests on bound materials at different size ratios D_2/D_1, $\sigma_n = 400$ kPa.
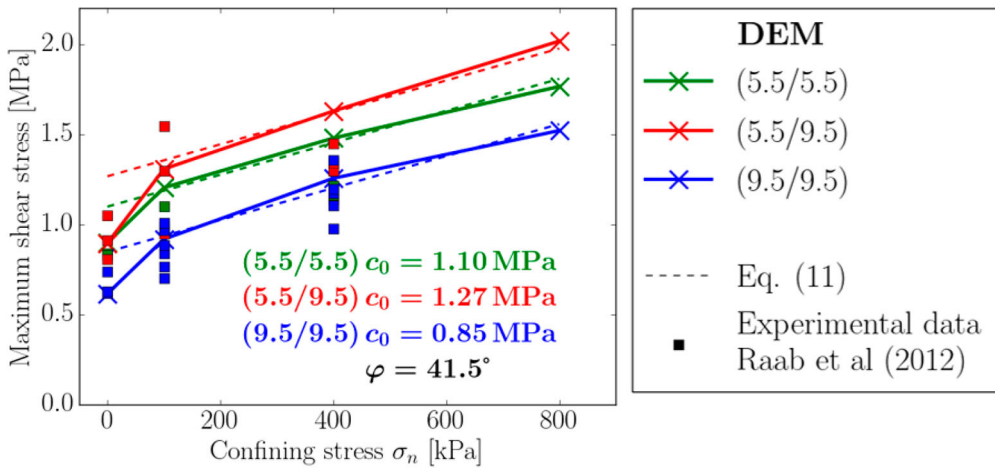

Figure 12. Maximum shear stress in simulated shear box tests on bound materials as a function of σ_n.

strength, a brief parametric study outlined in section 2 was performed, and the results are summarised in Figures 11 and 12.

In Figure 11, the effect of the particle size ratio between the upper (D_2) and bottom (D_1) layers on the interlayer strength is examined, for the cases summarised in Table 2. The results in Figure 10 are presented for the confining pressure of 400 kPa. The shear strength evolution in case of 100 kPa confining stress was found to follow the same trend and was therefore omitted here for clarity. Further, in Figure 11 the shear strengths of the (5.5/5.5), (9.5/9.5) and (5.5/9.5) materials are included for comparison. As seen in Figure 11, for $0.5 \leq D_2/D_1 \leq 1$ decreasing the particle size of the upper layer results in an increase of interlayer shear strength due to improved particle interlock as discussed qualitatively in connection to Figure 1. However, at $D_2/D_1 < 0.5$, further decrease of particle sizes in the upper layer has a profound negative effect on strength, which remains almost constant at $D_2/D_1 \leq 0.37$. This may be explained by particles becoming too small for being effectively embedded in both upper and bottom layers and are accordingly compromising the interlock properties. This observation also agrees

well with practice where $D_2/D_1 = 0.5$ proofed to be the most relevant nominal maximal aggregate size ratio between surface and binder courses.

It should be pointed out that the ratio D_2/D_1 does not uniquely determine the shear strength of the materials. In particular, for $D_2/D_1 = 1$, the strengths of three materials (5.5/5.5), (9.5/9.5) and (10/10) are shown in Figure 11, and it may be seen that decreasing particle size results in a significant increase of shear strength. This is somewhat expected as smaller particle sizes result in higher number of contact points and, accordingly, in more bonds per unit area. It is also of interest that, for the range of D_2/D_1 investigated, the minimum shear strength is observed at $D_2/D_1 = 1.33$, i.e. when the upper layer is composed of clearly coarse particles as compared to the bottom one.

In Figure 12, the effect of confining stress on the shear strength of (5.5/5.5), (9.5/9.5) and (5.5/9.5) materials is examined. Experimental shear strengths of the model material as measured by Raab et al. (2012) at $\sigma_n = 0$ kPa and 100, 400 kPa with Leutner (only bound material) and shear box test respectively are also presented in Figure 12 for comparison. In order to give an idea about the experimental scatter, the experimental results are presented as points corresponding to individual measurements. As shown in Figure 12, the calculated shear strength values agree reasonably well with the experiments and are definitely within experimental scatter. For all three materials, the shear strength increases linearly with pressure for all pressures above 100 kPa. This linear trend suggests that the increase in strength is governed primarily by frictional interactions, as the tangential force for initiating sliding is linearly proportional to the applied normal load. In order to illustrate this point further, linear fits to the strength values calculated for each material, in form of a Coulomb failure law

$$\tau_{max} = c_0 + \sigma_n \tan \varphi \qquad (3)$$

are also included in Figure 12. The angle φ is the same for all cases while, evidently, different cohesion values c_0 are used for the different size ratios.

At normal confining stress $\sigma_n = 0$ kPa the (9.5/9.5) material has a strength of 0.6 MPa which is approximately 50% lower compared to the values calculated for the (5.5/5.5) and (5.5/9.5) materials, which may be explained similarly to the discussion of Figure 10 by the higher number of bonds existing when smaller particles are present. Furthermore, for all three materials the strength increases fast between $\sigma_n = 0$ kPa and $\sigma_n = 100$ kPa, which is also in line with the experimental results by Raab et al. (2012). This rapid increase is attributed to the normal confining stress contributing to particle interlock by squeezing the two layers into each other. This effect may be expected to be most pronounced at the initial increase of normal stress.

4. Conclusions

In this study, the effects of particle interlock and particle contact conditions on interlayer strength were investigated through experimental and numerical modelling. The interlayer shear strength of materials composed of stiff binder blended with steel balls of different sizes was investigated experimentally. It is shown that the measurements on this simplified model materials capture the main features of interlayer response to shear loads. In particular, the effects of normal stress and of particle interlock on interlayer strength are well captured by the tests. At the same time, using the simplified representation of aggregates allows to remove at least some uncertainties associated with testing of real asphalt mixtures, such as associated with variable shape of aggregates, their mechanical properties, etc.

A Discrete Element method (DEM) model of the shear box test was developed, incorporating granular mechanics-based particle contact laws developed in earlier studies by the authors. The measurements on the model material were used to calibrate the contact law parameters as well as to validate the model. It was shown that the developed model captures adequately the measured force-displacement response of specimens. In particular, the effects of particle size combinations and of normal confining stress agrees well with experimental measurements. For the majority of cases the deviations between experiments and simulations are within experimental scatter.

Furthermore, combining experimental and numerical modelling allows to formulate simplified models as basis for real world considerations. In this study, the model was used to obtain an idea about the optimal relationship between the maximum aggregate size of two asphalt courses applied hot on cold with respect to the static interlayer shear strength. It may serve as a starting point for mechanical studies on real cases both with respect to optimal relative aggregate sizes of two pavement layers and optimal milling or textures of the layers. The developed model is also a feasible starting point for in depth numerical and experimental studies on the role of binder and tack coat with respect to interlayer shear strength of real asphalt layers. Such a development will, however, require further extension of contact laws in order to incorporate viscoelastic properties of the binder and its rate-dependent strength.

Disclosure statement

No potential conflict of interest was reported by the author(s).

ORCID

Denis Jelagin http://orcid.org/0000-0002-0596-228X
Erik Olsson http://orcid.org/0000-0001-7674-8582
Manfred N. Partl http://orcid.org/0000-0002-1041-0244

References

Ascher, D., & Wellner, F. (2007). Untersuchungen zur Wirksamkeit des Haftverbundes und dessen Auswirkungen auf die Lebensdauer von Asphaltbefestigungen. Technical University of Dresden, Germany, Report No. 13589 BR/1, 100 pages. (in German).

Canestrari, F., Attia, T., Di Benedetto, H., Graziani, A., Jaskula, P., Kim, Y. R., Maliszewski, M., Pais, J., Petit, C., Raab, C., Ragni, D., Rys, D., Sangiorgi, C., Sauzéat, C., & Zofka, A. (2021). Interlaboratory test to characterize the cyclic behavior of bituminous interlayers: An overview of testing equipment and protocols. In H. Di Benedetto, H. Baaj, E. Chailleux, G. Tebaldi, C. Sauzeat, & S. Mangiafico (Eds.), *Proceedings of the RILEM International Symposium on Bituminous Materials ISBM Lyon 2020* (pp. 29–36). Springer.

Canestrari, F., Ferrotti, G., Lu, X., Millien, A., Partl, M. N., Petit, C., Phelipot-Mardele, A., Piber, H., & Raab, C. (2013). Mechanical testing of interlayer bonding in asphalt pavements. In Advances in Interlaboratory Testing and Evaluation of Bituminous Materials, RILEM State-of-the-Art Reports Volume 9, 2013, ISBN: 978-94-007-5103-3 (Print) 978-94-007-5104-0 (Online), (pp. 303–360). doi:10.1007/978-94-007-5104-0.

Cundall, P. A., & Strack, O. D. L. (1979). A discrete numerical model for granular assemblies. *Géotechnique*, *29*(1), 47–65. https://doi.org/10.1680/geot.1979.29.1.47

Diakhaté, M., Phelipot, A., Millien, A., & Petit, C. (2006). Shear fatigue behaviour of tack coatsin pavements. *Road Materials and Pavement Design*, *7*(2), 201–222. https://doi.org/10.1080/14680629.2006.9690033

Ferrotti, G. (2007). *Experimental characterization of interlayer shear resistance in flexible pavements* [Doctoral dissertation]. Università Politecnica delle marche.

Ghafoori Roozbahany, E., & Partl, M. N. (2019). Investigation of asphalt joint compaction using discrete element simulation. *Road Materials and Pavement Design*, *20*(7), 1722–1734. https://doi.org/10.1080/14680629.2019.1594055

Gudmundson, P., & Larsson, P. L. (2021). An analytic model for effective mechanical properties and local contact stresses in lithium-ion porous electrodes. *Extreme Mechanics Letters*, *42*, 101067. https://doi.org/10.1016/j.eml.2020.101067

Hertz, H. (1881). Über die Berührung fester elastischer Körper. *Journal Für Die Reine Und Angewandte Mathematik*, *92*, 156–171.

Leutner, R. (1979). Untersuchungen des Schichtenverbundes beim bituminösen Oberbau. *Bitumen*, *3*, 84–91. (in German).

Mindlin, R. D. (1949). Compliance of elastic bodies in contact. *Journal of Applied Mechanics*, *16*(3), 259–268. https://doi.org/10.1115/1.4009973

Olsson, E., Jelagin, D., & Partl, M. N. (2019). New discrete element framework for modelling asphalt compaction. *Road Materials and Pavement Design*, *20*(S2), 604–616. https://doi.org/10.1080/14680629.2019.1633750

Olsson, E., Jelagin, D., & Partl, M. N. (2020). *Numerical evaluation of crushing resistance of unbound road material*. In Proceedings of the 9th International Conference on Maintenance and Rehabilitation of Pavements—Mairepav9 (pp. 201–, 210)., MAIREPAV9 1-3 July 2020,Springer, Cham.

Olsson, E., & Larsson, P. L. (2014). On the tangential contact behavior at elastic–plastic spherical contact problems. *Wear*, *319*(1-2), 110–117. https://doi.org/10.1016/j.wear.2014.07.016

Raab, C., Abd El Halim, A. O., & Partl, M. N. (2012). Interlayer bond testing using a model material. *Construction and Building Materials*, *26*(1), 190–199. https://doi.org/10.1016/j.conbuildmat.2011.06.009

Raab, C., Abd El Halim, A. O., & Partl, M. N. (2013). Utilisation of artificial neural network for the analysis of interlayer shear properties. *Baltic Journal of Road and Bridge Engineering*, *8*(2), 107–116. https://doi.org/10.3846/bjrbe.2013.14

Raab, C., & Partl, M. N. (1998). Shear strength properties between asphalt pavement layers. *Archives of Civil Engineering*, *XLIV*(33), 353–366.

Raab, C., Partl, M. N., & Abd El Halim, A. O. (2009). Evaluation of interlayer shear bond devices for asphalt pavements. *Baltic Journal of Road and Bridge Engineering*, *4*(4), 176–195. https://doi.org/10.3846/1822-427X.2009.4.186-195

Salinas, A., Al-Qadi, I. L., Hasiba, K. L., Ozer, H., Leng, Z., & Parish, D. C. (2013). Interface layer tack coat optimization,: transportation research record. *Journal of the Transportation Research Board*, *2372*(-1), 53–60. https://doi.org/10.3141/2372-07

Santagata, F. A., Partl, M. N., Ferrotti, G., Canestrari, F., & Flisch, A. (2008). Layer characteristics affecting interlayer shear resistance in flexible pavements. *Journal of the AAPT*, *77*, 22–254.

Storåkers, B., Biwa, S., & Larsson, P. L. (1997). Similarity analysis of inelastic contact. *International Journal of Solids and Structures*, *34*(24), 3061–3083. https://doi.org/10.1016/S0020-7683(96)00176-X

Thornton, C., Cummins, S. J., & Cleary, P. W. (2011). An investigation of the comparative behaviour of alternative contact force models during elastic collisions. *Powder Technology*, *210*(3), 189–197. https://doi.org/10.1016/j.powtec.2011.01.013

Wellner, F., & Wistuba, M. (2016). Zyklische Schersteifigkeits- und Scherermüdungsprüfung zur Bewertung und Optimierung des Schichtenverbundes in Strassenbefestigungen aus Asphalt. Bericht zu IGF-Vorhaben Nr. 17634 BG der Forschungsvereinigung Deutsches Asphaltinstitut (DAI) e.V. (in German).

Zhang, X., & Vu-Quoc, L. (2007). An accurate elasto-plastic frictional tangential force–displacement model for granular-flow simulations: Displacement-driven formulation. *Journal of Computational Physics*, *225*(1), 730–752. https://doi.org/10.1016/j.jcp.2006.12.028

Zofka, A., Maliszweski, M., Bernier, A., Josen, R., Vaitkus, A., & Kleiziene, R. (2015). Advanced shear tester for evaluation of asphalt concrete under constant normal stiffness conditions. *Road Materials and Pavement Design*, *16*(1), 187–210. https://doi.org/10.1080/14680629.2015.1029690